Applied Surface Science 578 (2022) 151982

Contents lists available at ScienceDirect

Applied Surface Science

journal homepage: www.elsevier.com/locate/apsusc

Full Length Article

Atomic layer deposited aluminum oxynitride coating for high-performance Si anode in lithium-ion batteries

Hongzheng Zhu [a], Mohammad Hossein Aboonasr Shiraz [a], Liang Liu [a,b], Yue Zhang [a], Jian Liu [a,*]

[a] School of Engineering, Faculty of Applied Science, University of British Columbia, Kelowna, BC V1V 1V7, Canada
[b] Automotive Engineering Research Institute, Jiangsu University, Zhenjiang 212013, China

ARTICLE INFO

Keywords:
Silicon anode
Aluminum oxynitride
Lithium-ion batteries
Atomic layer deposition

ABSTRACT

Silicon (Si) has received great attention as a promising anode material for lithium-ion batteries (LIBs) due to its high gravimetric capacity and large abundance. However, the use of Si anodes in LIBs has been hindered by their inferior electrochemical performance, resulting from its vast volume expansion and unstable solid electrolyte interphase (SEI). To address these problems, a novel surface coating material, aluminum oxynitride (AlO_xN_y), was developed using a plasma-enhanced atomic layer deposition technique with trimethylaluminum and plasma N_2/H_2 as the precursors. The effects of AlO_xN_y surface coatings on the electrochemical properties of Si electrodes were investigated. With the optimal AlO_xN_y coating (~2 nm), the reversible capacity after 140 cycles was improved from 331 mAh g^{-1} for bare Si electrode to 1297 mAh g^{-1} for AlO_xN_y-coated one, and the capacity retention was elevated from 13% to 72%. Post-cycling analysis revealed that the AlO_xN_y coating significantly suppressed the charge transfer and SEI resistances and maintained the structural integration of Si electrodes by suppressing continuous electrolyte decomposition and electrode delamination from the current collector. This study provides a new perspective on designing advanced functional coating materials for atomic layer deposition for lithium-ion batteries.

1. Introduction

Nowadays, the demand for lithium-ion batteries (LIBs) is increasing in many different fields, such as electronic devices, electric vehicles, and grid storage, due to their relatively high energy density and long lifetime among energy storage technologies available today. However, the ever-increasing need from end-users calls for LIBs with higher energy densities. In current commercial LIBs, graphite is used as the anode and possesses a theoretical capacity of 372 mAh g^{-1}, corresponding to 1-mol Li-ion per 6-mol C atoms. The low specific capacity of graphite results in limited energy densities of current LIBs and becomes one of the main limiting factors towards higher-performance LIBs [1–3]. Besides, present LIBs have serious safety concerns due to potential lithium plating on the graphite surface, and graphite anode needs to be replaced with a better anode with a higher specific capacity and working voltage [4]. Among all anode alternatives, Silicon (Si) has drawn the most attention because of its superior gravimetric capacity of 3590 mAh g^{-1} ($Li_{15}Si_4$) and high abundance on earth. It provides a tremendous increment to graphite [5–7].

However, Si experiences considerable volume change (~300%) during the charge and discharge process and thus suffers from severe capacity degradation, unstable solid electrolyte interphase (SEI), and low efficiency. For example, Si active material will pulverize due to the stress-induced by alloying and dealloying, causing rapid material degradation. The pulverization of Si materials also causes detachment and isolation of the Si electrode from the current collector. The successive formation-breaking-reformation procedure of SEI also leads to low Coulombic efficiency (CE), permanent consumption of electrolytes, and severe capacity drop for extended cycling [6,8–16]. All of the issues stem from the volume expansion of different phases of Li_xSi_y alloys and side reactions between these Li_xSi_y alloys with electrolytes during the lithiation/de-lithiation process. Several methods have been employed to tackle these issues, such as surface coating, nanosizing, and Si/graphite compositing. Utilizing surface coating on nanostructured Si to construct a physical compartment to buffer the volume expansion has been proven as a practical approach [17,18].

Among various surface coating methods, atomic layer deposition (ALD) has been an effective approach to create a protective layer on Si electrodes. ALD provides consecutive, separated, and self-terminating reactions between different chemical precursors and thus excellent

* Corresponding author.
E-mail address: Jian.liu@ubc.ca (J. Liu).

https://doi.org/10.1016/j.apsusc.2021.151982
Received 26 July 2021; Received in revised form 5 November 2021; Accepted 18 November 2021
Available online 20 November 2021

control over the uniformity and thickness of thin films at an atomic level. ALD enables highly uniform and conformal films on the complex surface due to its surface-controlled nature. The coating material usually serves an artificial SEI to prevent unexpected side reactions at the Si electrode/electrolyte interface and enhance battery performance. Many different types of coating have been applied on Si electrodes using ALD, such as metal oxides (Al_2O_3 and TiO_2) and metal nitride (TiN) [19]. In addition to these materials, metal oxynitride is another group of new materials with various properties, making it promising as surface coatings in batteries. For example, aluminum oxynitride (AlO_xN_y) has many excellent physical and chemical properties, which result in a wide range of electrical and optical responses [20]. These properties make AlO_xN_y potentially invaluable for many different areas, such as temperature sensors, transparent armor, military aircraft lenses and missile domes, and semi-conductor processing applications [21–23]. However, there is little research work on the development of surface chemistry and deposition process of AlO_xN_y by ALD and applications in batteries [24].

Herein, we adopted plasma-enhanced atomic layer deposition (PEALD) to deposit AlO_xN_y coating on the Si electrode for the first time. PEALD has been known as an enabler for a wide range of rapidly gaining applications in popularity. Several merits have been derived from PEALD compared to the thermal ALD. PEALD allows more flexibility in processing conditions and material properties and provides a high reactivity of the plasma species on the deposition surface. We developed AlO_xN_y coating by PEALD and applied it on the Si electrode in our work. By employing it as a surface modification, the confinement of silicon nanoparticles embedded into the electrode matrix is well achieved, while the kinetics of the charge/discharge process is enhanced due to the unique mechanical and electrical properties of AlO_xN_y films. The capacity retention of the Si electrode was elevated from 13.3% to 72.3% with the AlO_xN_y coating. The AlO_xN_y-coated Si electrode remains a reversible capacity of 1297 mAh g^{-1} after 140 cycles.

2. Experimental

2.1. Materials preparation

Si electrode was prepared by mixing Si nanoparticles (50-nm diameter, Alfa Aesar), Super P, and carboxymethyl cellulose/styrene-butadiene rubber (CMC/SBR) with a weight ratio of 7:2:1 in an aqueous solution to form a uniform slurry. Then the slurry was cast on a copper (Cu) foil and dried overnight in a vacuum oven at 80 °C.

AlO_xN_y coating was deposited on Si wafer and Si electrodes in a GEMStar XT-P PEALD system (Arradiance, USA). AlO_xN_y coating was directly applied on Si electrodes, because previous work has suggested that the ALD coating could form continuous protection layers on the whole surface of active material and conductive additives without impeding the electronic conduction network [25]. The deposition of AlO_xN_y was performed at 150 °C using trimethylaluminum (TMA) and plasma N_2/H_2 (50/50 sccm, plasma power 300 W) as the precursors. Each ALD cycle consisted of four steps: (1) 0.025-s pulse of TMA, (2) 10-s purge using Ar gas to remove TMA and any byproducts, (3) 10-s pulse of N_2/H_2 gases with exposure to plasma under 300 W power, and (4) 10-s purge with Ar gas. AlO_xN_y on the Si substrate was used for growth per cycle (GPC) and X-ray photoelectron spectroscopy (XPS) measurements. The thickness AlO_xN_y thin film shows a linear dependence on ALD cycles, yielding a growth per cycle (GPC) of 0.73 Å on Si wafer (Fig. SI-1). Si electrode coated with AlO_xN_y by 10, 30, and 50 ALD cycles were denoted as Si-AlO_xN_y-10, Si-AlO_xN_y-30, and Si-AlO_xN_y-50, respectively. Si wafer was also adopted as the substrate during the deposition for reference.

2.2. Structural characterizations

Morphology and structure of Si electrode and AlO_xN_y-coated Si electrodes were characterized by using a scanning electron microscope (SEM, Tescan MIRA3 FEG-ESEM) and high-resolution transmission electron microscopy (HRTEM, JEOL 2010F). X-ray photoelectron spectroscopy (XPS) was measured on an Axis Ultra DLD (Kratos Analytical).

2.3. Electrochemical characterizations

After AlO_xN_y coating, the electrode was cut into a round shape with a diameter of 12 mm and loaded into CR2032 cell configuration cells for electrochemical testing. The bare Si electrode and Si electrodes with AlO_xN_y coatings have been used the cathode, Li metal as the anode, and polyethylene (Celgard) as the separator. The electrolyte was 1.3 M $LiPF_6$ in ethylene carbonate: diethyl carbonate (EC: DEC, 3:7, *v/v*) with 10 vol % of fluoroethylene carbonate (FEC) as the additive.

The coin cells were assembled in an Ar-filled glove box with H_2O and O_2 concentrations below 0.1 ppm. The cycling performance of the coin cells was evaluated in a voltage range of 0.01–1.5 V and with five formation cycles at 0.05 C and subsequent cycles at 0.1 C, on a Neware BTS 4000 battery tester. Cyclic voltammetry (CV) and electrochemical impedance spectroscopy (EIS) were measured on a potentiostat/galvanostat/EIS workstation (SP-150, Biologic).

3. Results and discussion

Fig. 1 shows the structure and composition of Si nanoparticles coated with AlO_xN_y layer with 100 PEALD cycles. The TEM image in Fig. 1a reveals a uniform and conformal coating of AlO_xN_y film on the Si nanoparticles. The AlO_xN_y layer thickness is measured to be about 6.2 nm, slightly thinner than the value (7.3 nm) calculated based on a growth per cycle (GPC) of 0.73 Å on Si wafer substrate (Fig. SI-1). HRTEM observation discloses that the interplanar distance of the Si nanoparticle is 0.31 nm, corresponding to the (1 1 1) plane of Si (JCPDS No. 27-1402), as confirmed by the fast-Fourier-transform image in Fig. 1b inset. The AlO_xN_y layer on the Si nanoparticle surface possesses an amorphous structure and has no long-range order due to the low PEALD deposition temperature (150 °C). Fig. 1c presents a STEM image of Si nanoparticles with 100-cycle AlO_xN_y-coating and corresponding EDX mapping of Si and Al elements. STEM and EDX analysis prove the even distribution of AlO_xN_y coating on the surface of Si nanoparticles, suggesting the benefit of PEALD in achieving high-quality ultrathin layers on electrode materials. X-ray photoelectron spectroscopy (XPS) analysis confirms the existence of Al, O, and N elements from the AlO_xN_y coating on Si nanoparticles (Fig. 1d). Deconvolution of N1s peak leads to one peak located at 399.5 eV (Fig. 1e), ascribed to the N-Al-O bonding in aluminum oxynitride [26]. Al 2p spectrum is decomposed into one prominent peak at 74.6 eV, which corresponds to the Al-O bond and is verified by the 531.1 eV peak in the O 1s spectrum (Fig. 1e). The deconvolution of the O 1s spectrum resolves another peak centered at 532.1 eV, which could be assigned to the O-H bond. The residual O-H bond could result from incomplete removal of ligands from TMA on the outer surface during the PEALD process. The incorporation of the O element into AlO_xN_y might occur when the thin films are removed from the reaction chamber and exposed to the air. Previous work has suggested that metal nitrides can be quickly oxidized once direct exposure to air [27,28]. The oxidation of AlN could happen because of exposure to air when the samples were taken out of the ALD reaction chamber. The same phenomena were observed in PELAD TiN, which was proven as TiN_xO_y due to air exposure [29].

Fig. 2 depicts the effect of AlO_xN_y coatings (10, 30, and 50 ALD cycles) on the electrochemical performance of Si electrodes as an anode in LIBs. All cells are tested between 0.01 and 1.5 V at 0.05 C in the initial five cycles (formation) and 0.1 C in the subsequent cycles. The AlO_xN_y coating on Si electrodes was confirmed by EDX mapping under SEM (Fig. SI-2). As seen in Fig. 2 (a), the initial discharge capacity is 3094 mAh g^{-1} for bare Si, and 2108, 2357, and 1624 mAh g^{-1} for the Si electrodes with 10-cycle, 30-cycle, and 50-cycle AlO_xN_y coating, respectively. The higher discharge capacity of bare Si than the others in

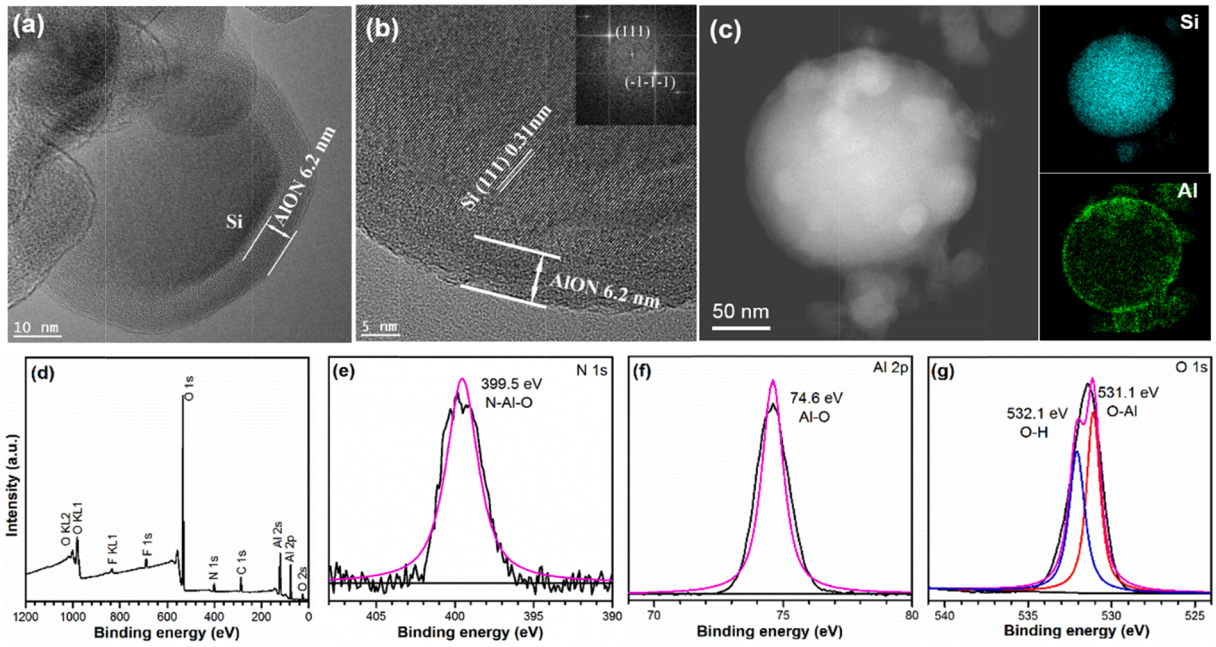

Fig. 1. (a) TEM image, (b) HRTEM image, and (c) STEM image with EDX mapping of Si and Al elements for Si particles with AlO_xN_y coating deposited by 100 ALD cycles, (d) XPS full survey and deconvolution of (e) N 1s, (f) Al 2p, and (g) O 1s spectra of AlO_xN_y thin film on a Si substrate. (Inset in (b) is the Fast Fourier transform (FTT) image of the Si particle).

the initial cycles can be attributed to the higher availability of Si particles to react with Li-ion than those of coated ones. In the AlO_xN_y-coated electrode, Li-ions need to interact with AlO_xN_y first to pass through the coating layer and then undergo alloying reactions with Si particles. From the 6th cycle, the Si electrodes with and without AlO_xN_y coatings exhibit a dramatic difference in the specific capacity and cycling stability. The discharge capacity of Si-AlO_xN_y-10, Si-AlO_xN_y-30, and Si-AlO_xN_y-50 stabilizes at 1355, 1664, and 1070 mAh g^{-1}, respectively, while the specific capacity of bare Si rapidly drops to 937 mAh g^{-1} in the 6th cycle. The bare Si undergoes much more degradation during the initial ten cycles than those with AlO_xN_y coatings, probably due to continuous breakdown and formation of SEI layers on Si surface [30]. Among all the samples, Si-AlO_xN_y-30 maintains the highest specific capacity of 1297 mAh g^{-1} after 140 cycles, in contrast to 331 mAh g^{-1} of bare Si, demonstrating enhanced electrochemical properties of Si electrode using thin AlO_xN_y coating (~2 nm thick) by PEALD. The capacity retention of Si electrodes (140th-cycle capacity/2nd-cycle capacity) is elevated from 13% to 72% by using AlO_xN_y coating. From Fig. 2a, it can be found that the electrochemical performance of Si electrodes has a strong dependence on the thickness of AlO_xN_y coatings. The optimal one is the Si electrode with a 30-ALD cycle AlO_xN_y coating (~2 nm). Si electrode with 50-ALD cycle AlO_xN_y layer still shows stable cycling stability but experiences a noticeable decrease in its specific capacity compared to Si-AlO_xN_y-30. The reason could be that AlO_xN_y coating is too thick and reduce the diffusion rate of Li ions through the artificial SEI layer, leading to suppressed redox reactions in the Si anode.

CE in the 2nd cycle is calculated as 69.9% and 93.9% for the pristine Si and Si-AlO_xN_y-30, respectively, implying that AlO_xN_y coating reduces the side reaction between the Si electrode and the electrolyte. In general, AlO_xN_y-coated Si electrodes show improved and stabilized CE over repeated cycling, while pristine Si electrode exhibits high fluctuation in the CE (Fig. 2b). A direct comparison between the charge–discharge curves for pristine Si and Si-AlO_xN_y-30 is presented in Fig. 2c and d. Pristine Si experiences gradual degradation in the specific capacity and increased polarization, as evidenced by the enlarged charge–discharge plateaus. In contrast, the charge–discharge profiles for Si-AlO_xN_y-30 have good overlap in the 1st, 2nd, 3rd, 10th, and 50th cycles, suggesting the importance of surface coating in preventing side reactions on the Si surface.

To investigate the improved electrochemical properties of Si electrode by AlO_xN_y coating, the CV test was applied on the electrodes at the scan rate of 0.2 mV s^{-1}, and the result is shown in Fig. 2 (e) and (f). In the first cycle, it is clear that the reduction curve of bare Si has a shoulder peak at 0.8 V, corresponding to the formation of the SEI layer on the non-coated electrode in the initial cycle. This SEI formation is the direct consequence of the electrolyte decomposition and active Si loss, leading to the lower capacity of the pristine Si electrode. In contrast, the AlO_xN_y-coated electrode shows a significantly suppressed shoulder, indicating the effective role of thin AlO_xN_y film to suppress the direct contact of active Si metal with electrolyte while providing a facile Li-ion pathway to react with Si particles in lithiation/de-lithiation. Meanwhile, the separation between oxidation and reduction peaks of Si is reduced with a 30-cycle AlO_xN_y coating, indicating better kinetics in the Si-AlO_xN_y-30 electrode. A better overlapping of oxidation–reduction peaks, especially at the charge/discharge switch point, is observed in Si-AlO_xN_y-30, suggesting a better kinetic and suppressing thick SEI layer formation-repeated silicon exfoliation with AlO_xN_y coating. This good overlapping is consistent with the charge–discharge curves in Fig. 2d. Thus, this rigid coating layer is crucial for alloying/dealloying electrodes, which are accompanied by dramatic volume change upon the lithiation/de-lithiation process.

To have a better understanding of the mechanism of AlO_xN_y-coating on Si electrode, the electrochemical impedance spectroscopy (EIS) analysis was performed on Si electrodes with different AlO_xN_y coatings before and after 100 battery cycles. As shown in Fig. 3 (a), before cycling, the cell displays a single semicircle at the high frequency, corresponding to the charge-transfer resistance of the anode surface and the electrolyte, and a straight line at the low frequency, representing the Warburg resistance. Compared to the pristine Si electrode, AlO_xN_y-coated Si electrodes show reduced charge transfer and solution resistances (Fig. 3), probably due to the good electrical conductivity of AlO_xN_y coating layer. Si-AlO_xN_y-10 exhibits the smallest charge-transfer resistance of 100 Ω, compared to 142 Ω for bare Si electrode (Table 1).

In Fig. 3 (b), all the electrode after cycling shows two semicircles in the high-frequency range, which represent the charge-transfer resistance and SEI resistance, respectively. As seen, AlO_xN_y coated Si

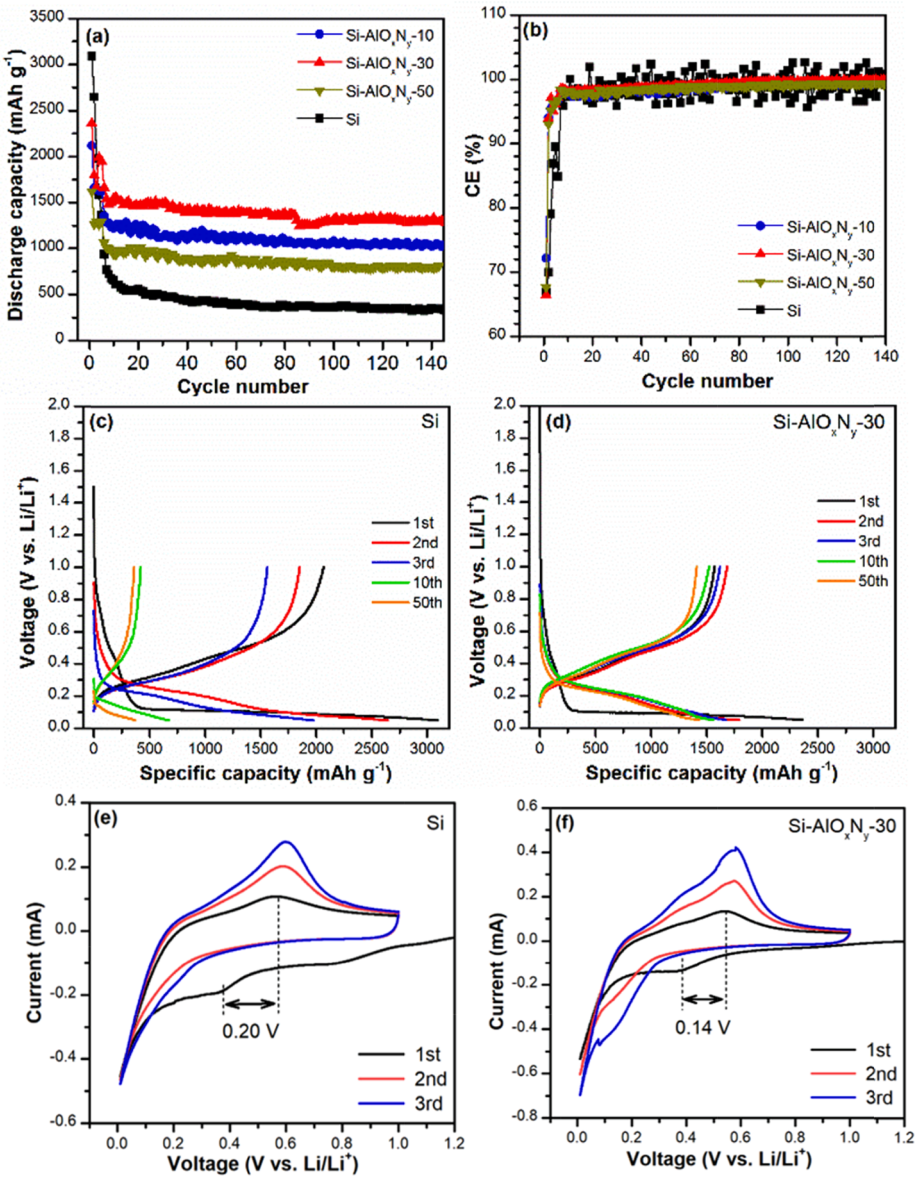

Fig. 2. (a) Cycling stability and (b) Coulombic efficiency (CE) of bare Si electrode and Si electrode coated with AlO_xN_y layers by 10, 30, and 50 ALD cycles, measured between 0.01 and 1.5 V at 0.05 C during the initial five cycles and 0.1 C in the subsequent cycles; (c, d) charge–discharge profiles and (e, f) Cyclic voltammetry (CV) curves measured at 0.2 mV s^{-1} for Si and Si-AlO_xN_y-30 electrodes.

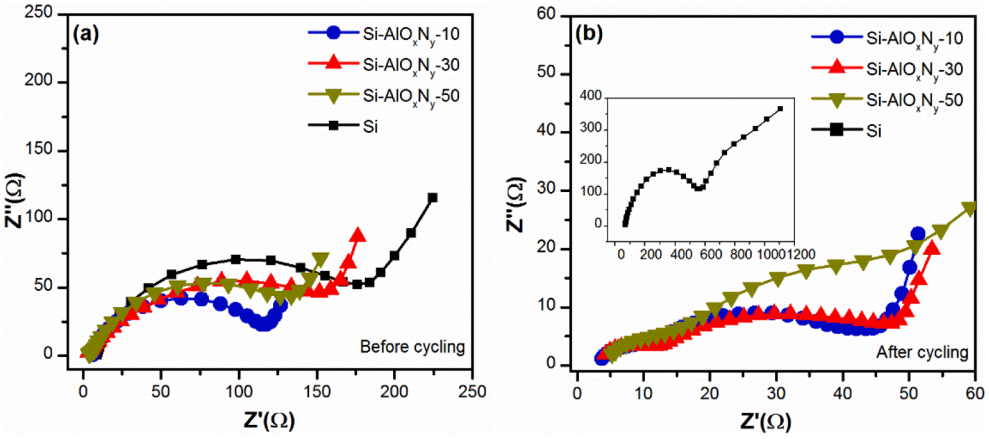

Fig. 3. Nyquist plots of bare Si electrode and Si electrodes coated with AlO_xN_y layers by 10, 30, and 50 ALD cycles (a) before cycling and (b) after 100 charge/discharge cycles.

Table 1
Fitting result of Nyquist plots in Fig. 3 for Si electrodes with different AlO_xN_y layers before and after 100 charge/discharge cycles.

Electrode	Before cycling		After cycling		
	R_s (Ω)	R_{ct} (Ω)	R_s (Ω)	R_f (Ω)	R_{ct} (Ω)
Si	8.0	142.0	65.9	485.1	370.6
Si-AlO_xN_y-10	5.5	100.0	3.1	30.0	6.4
Si-AlO_xN_y-30	2.0	134.0	3.1	30.0	7.3
Si-AlO_xN_y-50	3.0	114.0	3.6	12.1	18.4

electrodes display significantly smaller semicircles in the medium frequency range, suggesting the decreased SEI resistances with AlO_xN_y coating. As a result, we can see, in the coated sample, the artificial SEI layer improved the kinetic of the coated Si electrode, which leads to better cycling performance, CE, and capacity retention.

The Nyquist profiles are fitted by using the equivalent circuit before cycling ($R_s(R_{ct}Q)W$) and after cycling ($R_s(R_fQ)(R_{ct}Q)W$) to obtain EIS parameters (Table 1). R_s, R_f, and R_{ct} represent the resistance of solution (electrolyte), SEI layer, and charge transfer, respectively. Q and W parameters are constant-phase element and Warburg resistance, respectively.

Fig. 4 shows the morphologies of the Si electrodes with and without AlO_xN_y coating before and after 100 charge–discharge cycles. Fig. 4 (a) and (b) show that the surface of cycled Si electrode has severe delamination because of Si swelling during the repeated battery charge and discharge processes. Fig. 4 (b) indicates that the Si active material has been detached from the Cu current collector, responsible for the fast decay in its electrochemical battery performance. In contrast, the surface morphology of the cycled AlO_xN_y-coated electrode (Fig. 4 (d)) maintains the original structure of the fresh electrode (Fig. 4 (c)), with only little cracks. In the cross-section image, it can be found that the Si active material (Fig. 4(d)) is strongly attached to the Cu current collector, leading to the stable and excellent electrochemical performance of the AlO_xN_y coated electrode due to the confinement effect of AlO_xN_y in Si volume expansion.

The compositions of SEI layers on Si electrodes with and without AlO_xN_y coating are examined using XPS and the results are presented in Fig. 5. Fig. 5 (a) shows the XPS results of the cycled Si electrode with and without AlO_xN_y coating for the C1s peak. The C1s peak can be split into three individual peaks located at Li_2CO_3 (289.7 eV), C—O (286.2 eV), C—C (284.8 eV). Li_2CO_3 is a well-known electrolyte reduction product that comes from the irreversible formation of the SEI layer. Poor CE usually occurs with this reduction product [31]. As we can see in Fig. 5 (b), O 1s peak also proves the existence of Li_2CO_3. Meanwhile, in the Si electrode with AlO_xN_y (Fig. 5b), the Li_2O component is also detected at 530.5 eV. The signal for LiF in Fig. 5(c) is considered an electrolyte decomposition product from the $LiPF_6$ salt, which comes from battery cycling over time [32]. The LiF peak is relatively stronger in AlO_xN_y coated Si electrode than the bare Si electrode, attributed to the firm SEI layer on the electrode resulting in lower Si exposure. Fig. 5(d) shows the high-resolution XPS spectra of N1s peak from Si electrode without and with AlO_xN_y after cycling. For the Si-AlO_xN_y electrode after cycling, one peak can be located at Li-N bonding (399.7 eV) [33]. Li-N bonding confirms the presence of Li_3N on AlO_xN_y coated Si after cycling. Li_3N is an ion conductor with very high Li-ion conductivity ($\sigma > 1x10^{-3}$ S cm^{-1}), which comes from Li-ion transfer reaction through AlO_xN_y coating during cycling [34]. Meanwhile, Fig. 5(e) also confirms the Li-Al-O bonding, a well-known excellent Li-ion conductor [35]. The Li-Al-O comes from the Li-ion reaction with Al-O in AlO_xN_y coating. The artificial SEI layer contains Li_3N and Li-Al-O, which act as the Li-ion pathway to improve the ion transfers while maintaining the electrode

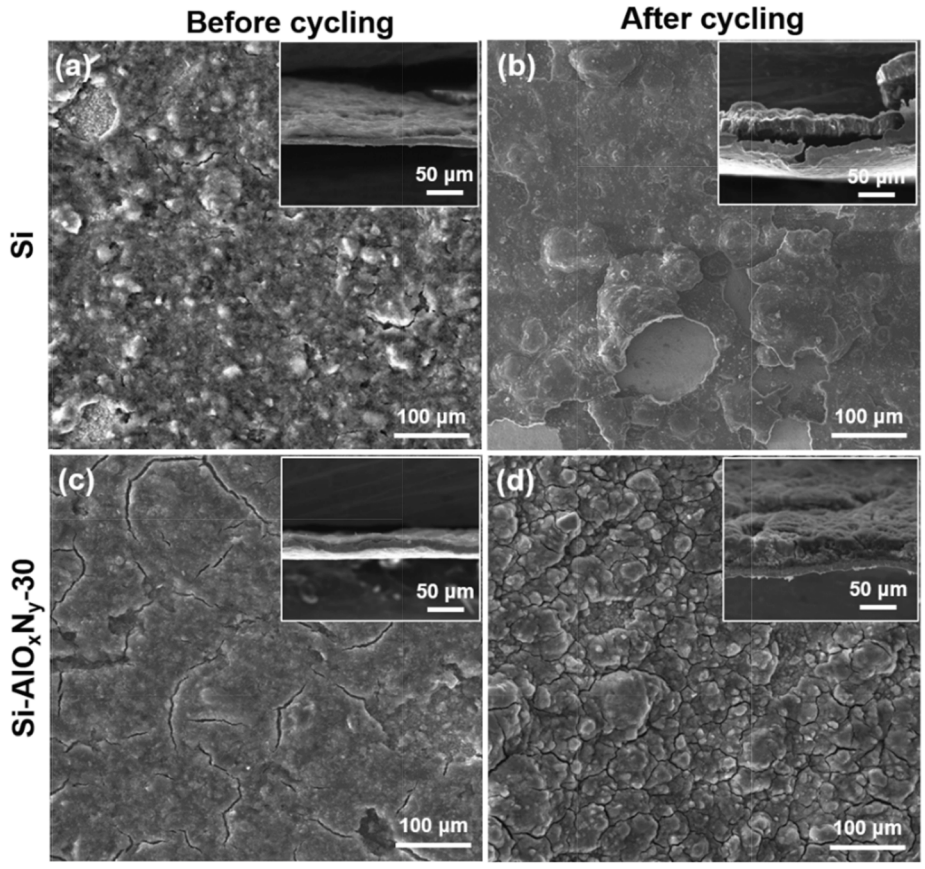

Fig. 4. The top-view and cross-section -view SEM images of (a, b) pristine Si electrode and (c, d) Si-AlO_xN_y-30 electrodes (a, c) before and (b, d) after 100 charge–discharge cycles.

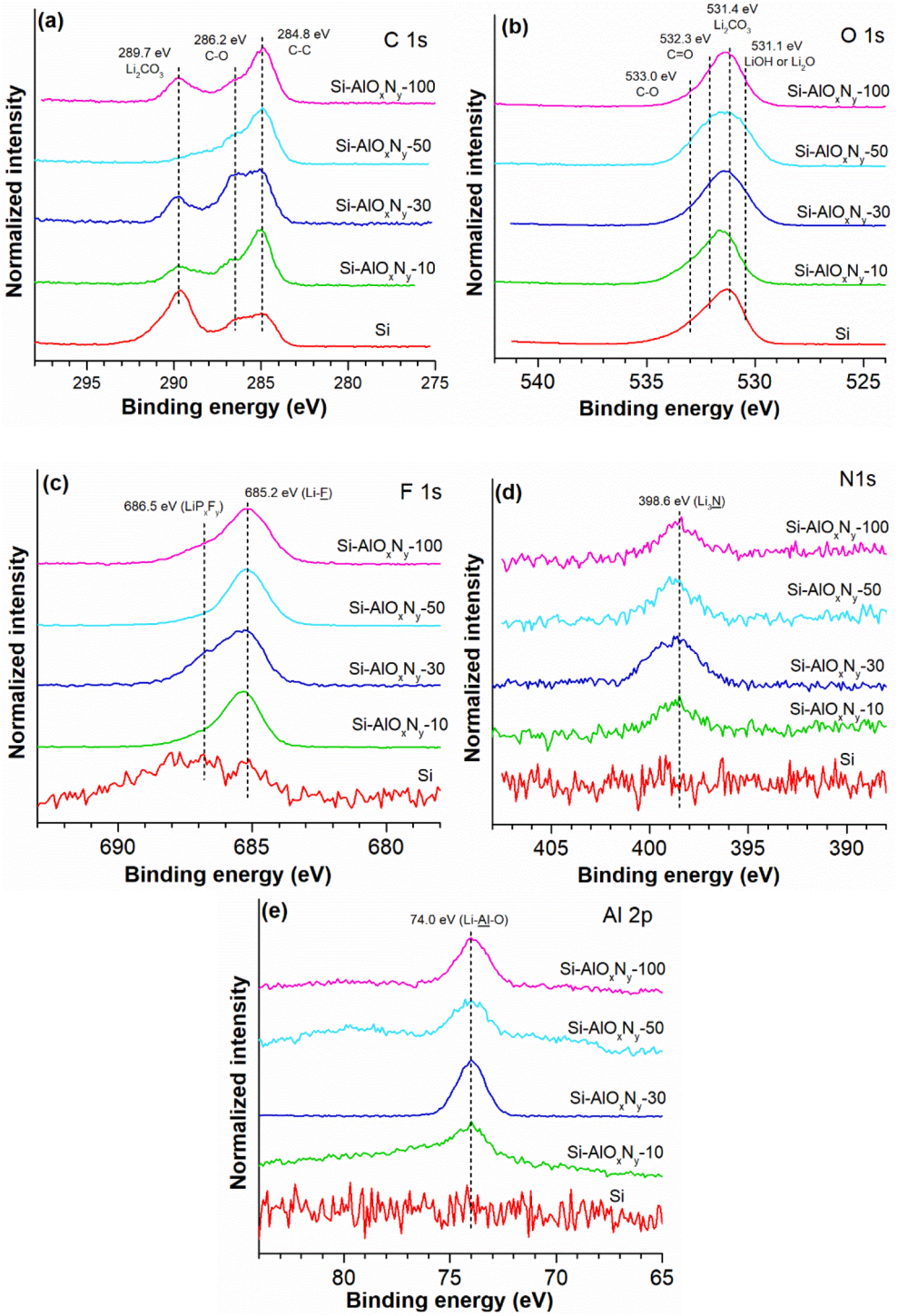

Fig. 5. (a) C 1s, (b) O 1s, (c) F 1s, (d) N1s and (e) Al 2p spectra of bare Si electrode and Si electrode coated with AlO_xN_y layers by 10, 30, and 50 ALD cycles after 100 battery cycles.

mechanical/structural architecture, meanwhile reduces the silicon expansion and lower the interaction of electrode–electrolyte at their interfaces.

For the AlO_xN_y-coated Si electrode, the reaction of Li-ion and AlO_xN_y coating over cycles creates an artificial SEI layer containing Li_3N according to the reaction of $4Li + AlN \rightarrow Li_3N + LiAl$ [36]. Li_3N is an ion conductor with very high Li-ion conductivity ($\sigma > 1x10^{-3}$ S cm^{-1}) [37]. The artificial SEI layer improved the coated Si electrode's capacity and kinetic, meanwhile reducing the silicon expansion and lowering the interaction of electrode–electrolyte at their interfaces. The artificial SEI layer performs as the Li-ion pathway to improve the ion transfers while maintaining the electrode mechanical/structural architecture.

The cycling stability of the Si electrode with and without AlO_xN_y coating was further examined at 55 °C, and the results are shown in Fig. 6 (a). The bare Si electrode exhibits higher discharge capacities than Si-AlO_xN_y-30 in the first three cycles because the AlO_xN_y coating layer is less active for Li-ion diffusion at the beginning and requires an "activation process" to become ion conductive. Therefore, the AlO_xN_y coating layer impedes the ion conduction in the first few cycles, leading to the reduced reversible capacities of Si-AlO_xN_y-30. The bare Si

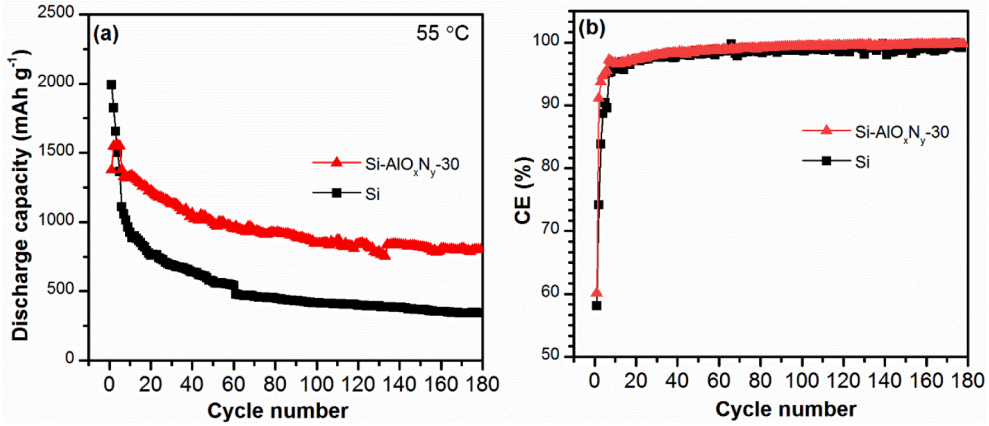

Fig. 6. (a) Cycling stability and (b) CE of Si electrodes with and without 30-cycle AlO_xN_y coating measured at 55 °C.

electrode shows a rapid capacity decay in 50 cycles, which is caused by the severe side reaction between Si and the electrolyte at the raised temperatures. As a result, the un-coated Si has capacity retention of 19.1% after 175 cycles. However, in contrast, Si-AlO_xN_y-30 exhibits much-improved cycle stability and capacity retention of 51.3% over 175 cycles. Furthermore, Si-30 possesses a relatively stable CE of 98–99% over cycling, while bare Si experiences a more fluctuated state in the CE. These results suggest the durable artificial SEI layers enabled by AlO_xN_y coating, which confirm the importance of AlO_xN_y coating to Si anode performances at higher temperatures.

4. Conclusions

In summary, Si electrodes were coated with AlO_xN_y thin films by PEALD for the first time and applied as the anode for lithium-ion batteries. The electrochemical performance was enhanced due to the electrochemical properties of AlO_xN_y film. The capacity retention of the AlO_xN_y-coated Si electrode was elevated to 72.3%, compared to 13.3% of bare Si electrode. The capacity remained 1297 mAh g^{-1} at 140 cycles, and capacity retention of 51.3% over 175 cycles at 55 °C, indicating promising cycle stability capability of AlO_xN_y-coated Si electrode. The electrochemical reaction mechanism study and XPS analysis revealed that Li-ion interaction with AlO_xN_y coating over cycles led to the formation of an artificial SEI layer containing Li_3N and Li-Al-O. The artificial SEI layer performed as the Li-ion pathway to improve the ion transfers while maintaining the electrode mechanical/structural architecture and improved the capacity and kinetic of the coated Si electrode. It also suppressed the silicon volume change and lowered the side reactions at the electrode–electrolyte interfaces. This work might open a new pathway to design high-performance Si electrode materials for Li-ion batteries.

CRediT authorship contribution statement

Hongzheng Zhu: Methodology, Validation, Investigation, Visualization, Writing – original draft. **Mohammad Hossein Aboonasr Shiraz:** Investigation. **Liang Liu:** Investigation. **Yue Zhang:** Investigation. **Jian Liu:** Visualization, Supervision, Funding acquisition, Writing – review & editing, Resources.

Declaration of Competing Interest

The authors declare that they have no known competing financial interests or personal relationships that could have appeared to influence the work reported in this paper.

Acknowledgements

This work was supported by the Nature Sciences and Engineering Research Council of Canada (NSERC), Canada Foundation for Innovation (CFI), BC Knowledge Development Fund (BCKDF), Mitacs Accelerate Program, MGX Minerals, and the University of British Columbia (UBC). The authors would like to thank Dr. Carmen Andrei at the Canadian Centre for Electron Microscopy (CCEM) at McMaster University for her assistance on HRTEM characterization.

Appendix A. Supplementary material

Supplementary data to this article can be found online at https://doi.org/10.1016/j.apsusc.2021.151982.

References

[1] A.S. Arico, P. Bruce, B. Scrosati, J.-M. Tarascon, W. Van Schalkwijk, Nanostructured materials for advanced energy conversion and storage devices, Mater. Sustain. Energy: Collect. Peer-rev. Res. Rev. Articles Nature Publ. Group (2011) 148–159.
[2] J.R. Owen, Rechargeable lithium batteries, Chem. Soc. Rev. 26 (4) (1997) 259–267.
[3] J.-M. Tarascon, M. Armand, Issues and challenges facing rechargeable lithium batteries,, Mater. Sustain. Energy: Collect. Peer-rev. Res. Rev. Articles Nature Publ. Group (2011) 171–179.
[4] Y.u. Chen, L. Liu, J. Xiong, T. Yang, Y. Qin, C. Yan, Porous Si nanowires from cheap metallurgical silicon stabilized by a surface oxide layer for lithium ion batteries, Adv. Funct. Mater. 25 (43) (2015) 6701–6709.
[5] J.R. Szczech, S. Jin, Nanostructured silicon for high capacity lithium battery anodes, Energy Environ. Sci. 4 (1) (2011) 56–72.
[6] H. Wu, Y.i. Cui, Designing nanostructured Si anodes for high energy lithium ion batteries, Nano Today 7 (5) (2012) 414–429.
[7] J.-Y. Li, Q. Xu, G.e. Li, Y.-X. Yin, L.-J. Wan, Y.-G. Guo, Research progress regarding Si-based anode materials towards practical application in high energy density Li-ion batteries, Mater. Chem. Front. 1 (9) (2017) 1691–1708.
[8] L.Y. Beaulieu, K.W. Eberman, R.L. Turner, L.J. Krause, J.R. Dahn, Colossal reversible volume changes in lithium alloys, Electrochem. Solid State Letters 4 (9) (2001) A137, https://doi.org/10.1149/1.1388178.
[9] J.H. Ryu, J.W. Kim, Y.-E. Sung, S.M. Oh, Failure modes of silicon powder negative electrode in lithium secondary batteries, Electrochem. Solid State Lett. 7 (10) (2004) A306, https://doi.org/10.1149/1.1792242.
[10] S.-H. Ng, J. Wang, D. Wexler, K. Konstantinov, Z.-P. Guo, H.-K. Liu, Highly reversible lithium storage in spheroidal carbon-coated silicon nanocomposites as anodes for lithium-ion batteries, Angew. Chem. Int. Ed. 45 (41) (2006) 6896–6899.
[11] J.W. Wang, Y.u. He, F. Fan, X.H. Liu, S. Xia, Y. Liu, C.T. Harris, H. Li, J.Y. Huang, S. X. Mao, T. Zhu, Two-phase electrochemical lithiation in amorphous silicon, Nano Lett. 13 (2) (2013) 709–715.
[12] M. Gu, Y. Li, X. Li, S. Hu, X. Zhang, W.u. Xu, S. Thevuthasan, D.R. Baer, J.-G. Zhang, J. Liu, C. Wang, In situ TEM study of lithiation behavior of silicon nanoparticles attached to and embedded in a carbon matrix, ACS Nano 6 (9) (2012) 8439–8447.
[13] X.H. Liu, L.i. Zhong, S. Huang, S.X. Mao, T. Zhu, J.Y. Huang, Size-dependent fracture of silicon nanoparticles during lithiation, ACS Nano 6 (2) (2012) 1522–1531.
[14] Z.-L. Xu, X. Liu, Y. Luo, L. Zhou, J.-K. Kim, Nanosilicon anodes for high performance rechargeable batteries, Prog. Mater Sci. 90 (2017) 1–44.

[15] Z.-L. Xu, B. Zhang, J.-K. Kim, Electrospun carbon nanofiber anodes containing monodispersed Si nanoparticles and graphene oxide with exceptional high rate capacities, Nano Energy 6 (2014) 27–35.
[16] J. Tang, Q. Yin, Q. Wang, Q. Li, H. Wang, Z. Xu, H. Yao, J. Yang, X. Zhou, J.K. Kim, L. Zhou, Two-dimensional porous silicon nanosheets as anode materials for high performance lithium-ion batteries, Nanoscale 11 (2019) 10984–10991.
[17] S.-B. Son, S.C. Kim, C.S. Kang, T.A. Yersak, Y.-C. Kim, C.-G. Lee, S.-H. Moon, J. S. Cho, J.-T. Moon, K.H. Oh, S.-H. Lee, A highly reversible nano-Si anode enabled by mechanical confinement in an electrochemically activated $Li_xTi_4Ni_4Si_7$ matrix, Adv. Energy Mater. 2 (10) (2012) 1226–1231.
[18] D.M. Piper, T.A. Yersak, S.-H. Lee, Effect of compressive stress on electrochemical performance of silicon anodes, J. Electrochem. Soc. 160 (1) (2013) A77–A81.
[19] E.M. Lotfabad, P. Kalisvaart, A. Kohandehghan, K. Cui, M. Kupsta, B. Farbod, D. Mitlin, Si nanotubes ALD coated with TiO_2, TiN or Al_2O_3 as high performance lithium ion battery anodes, J. Mater. Chem. A 2 (8) (2014) 2504–2516, https://doi.org/10.1039/c3ta14302c.
[20] S. Yang, H. Chen, J. Li, H. Guo, X. Mao, R. Tian, J. Zhang, S. Wang, Oxidation behavior and mechanism of aluminum oxynitride (AlON) at elevated temperatures, J. Am. Ceram. Soc. 104 (2) (2021) 1040–1046.
[21] J.C.S. Fernandes, M.G.S. Ferreira, Corrosion behaviour of tungsten-implanted aluminium in carbonate and sulphate solutions, Surf. Coat. Technol. 56 (1) (1992) 75–79, https://doi.org/10.1016/0257-8972(92)90198-J.
[22] J.C.S. Fernandes, R. Picciochi, M. Da Cunha Belo, T. Moura e Silva, M.G.S. Ferreira, I.T.E. Fonseca, Capacitance and photoelectrochemical studies for the assessment of anodic oxide films on aluminium, Electrochimica Acta 49 (26) (2004) 4701–4707, https://doi.org/10.1016/j.electacta.2004.05.025.
[23] J. Borges, C. Fonseca, N.P. Barradas, E. Alves, T. Girardeau, F. Paumier, F. Vaz, L. Marques, Influence of composition, bonding characteristics and microstructure on the electrochemical and optical stability of AlO_xN_y thin films, Electrochim. Acta 106 (2013) 23–34, https://doi.org/10.1016/j.electacta.2013.05.020.
[24] P.K. Parashar, S.A. Kinnunen, T. Sajavaara, J.J. Toppari, V.K. Komarala, Thermal atomic layer deposition of AlOxNy thin films for surface passivation of nano-textured flexible silicon, Sol. Energy Mater. Sol. Cells 193 (2019) 231–236.
[25] Y.S. Jung, A.S. Cavanagh, L.A. Riley, S.H. Kang, A.C. Dillon, M.D. Groner, S. M. George, S.H. Lee, Ultrathin direct atomic layer deposition on composite electrodes for highly durable and safe Li-ion batteries, Adv. Mater. 22 (2010) 2172–2176.
[26] X. Han, Z. Zhang, R. You, G. Zheng, C. Li, S. Chen, Y. Yang, Capitalization of interfacial AlON interactions to achieve stable binder-free porous silicon/carbon anodes, J. Mater. Chem. A 6 (17) (2018) 7449–7456, https://doi.org/10.1039/c8ta01029c.
[27] K.J. Chen, S. Huang, AlN passivation by plasma-enhanced atomic layer deposition for GaN-based power switches and power amplifiers, Semicond. Sci. Technol. 28 (7) (2013) 074015, https://doi.org/10.1088/0268-1242/28/7/074015.
[28] A.P. Perros, H. Hakola, T. Sajavaara, T. Huhtio, H. Lipsanen, Influence of plasma chemistry on impurity incorporation in AlN prepared by plasma enhanced atomic layer deposition, J. Phys. D Appl. Phys. 46 (50) (2013) 505502.
[29] Y. Zhang, Y. Wu, H. Ding, Y. Yan, Z. Zhou, Y. Ding, N. Liu, Sealing ZnO nanorods for deeply rechargeable high-energy aqueous battery anodes, Nano Energy 53 (2018) 666–674, https://doi.org/10.1016/j.nanoen.2018.09.021.
[30] K. Feng, W. Ahn, G. Lui, H.W. Park, A.G. Kashkooli, G. Jiang, X. Wang, X. Xiao, Z. Chen, Implementing an in-situ carbon network in Si/reduced graphene oxide for high performance lithium-ion battery anodes, Nano Energy 19 (2016) 187–197.
[31] X. Xiao, P. Lu, D. Ahn, Ultrathin multifunctional oxide coatings for lithium ion batteries, Adv. Mater. 23 (34) (2011) 3911–3915.
[32] K. Xu, Nonaqueous liquid electrolytes for lithium-based rechargeable batteries, Chem. Rev. 104 (10) (2004) 4303–4417, https://doi.org/10.1021/cr030203g.
[33] C.-H. Chang, S.-H. Chung, P. Han, A. Manthiram, Oligoanilines as a suppressor of polysulfide shuttling in lithium–sulfur batteries, Mater. Horiz. 4 (5) (2017) 908–914, https://doi.org/10.1039/c7mh00510e.
[34] T. Lapp, S. Skaarup, A. Hooper, Ionic conductivity of pure and doped Li3N, Solid State Ionics 11 (2) (1983) 97–103, https://doi.org/10.1016/0167-2738(83)90045-0.
[35] S.C. Jung, Y.-K. Han, How do Li atoms pass through the Al2O3 coating layer during lithiation in Li-ion batteries? J. Phys. Chem. Lett. 4 (16) (2013) 2681–2685, https://doi.org/10.1021/jz401231e.
[36] T. Kusunose, T. Sekino, Improvement in fracture strength in electrically conductive AlN ceramics with high thermal conductivity, Ceram. Int. 42 (11) (2016) 13183–13189, https://doi.org/10.1016/j.ceramint.2016.05.110.
[37] Z. Yan, X.-Y. Niu, X.-Q. Du, Q.-C. Wang, X.-J. Wu, Y.-N. Zhou, Activating AlN thin film by introducing Co nanoparticles as a new anode material for thin-film lithium batteries, Rare Met. 37 (8) (2018) 625–632, https://doi.org/10.1007/s12598-018-1013-2.